nature communications

Article

https://doi.org/10.1038/s41467-025-67020-z

Multiphase aqueous soggy sand electrolyte for zinc metal batteries applications at elevated temperatures

Received: 26 April 2025

Accepted: 18 November 2025

Published online: 04 December 2025

Check for updates

Jingxuan Ren[1,2,3], Jie Zhang[1,3], Yufeng Chen[1], Renming Liu[1], Chuangwei Liu[1], Xinli Guo[2], Dan Luo[1], Dongdong Wang[1] ✉ & Zhongwei Chen[1] ✉

Aqueous zinc metal batteries often encounter uncontrollable failure or performance decay under thermal environments, primarily due to the severe side reactions caused by aqueous electrolytes. Here, an organic-inorganic-H_2O multiphase aqueous soggy sand electrolyte is reported to enhance high-temperature performance of aqueous zinc metal batteries. Soggy sand components form strong interactions between the heterogeneous phases, reconstructing hydrogen-bond networks and forming water-deficient solvation structures, which greatly limits water activity and improves thermal stability, eliminating parasitic reactions and inspiring a uniform Zn deposition at elevated temperatures. As a result, multiphase aqueous soggy sand electrolyte enables aqueous zinc metal batteries to achieve an operating temperature of 140 °C, a lifespan of 1700 cycles, and a current density of 8 A g^{-1}. More importantly, the application of this electrolyte allows the stable cycling of Zn metal pouch cells under continuous operation at elevated temperatures. This work paves the path towards electrolyte design that enables aqueous batteries to cycle stably under thermal environments.

The exponential growth of modern industrial systems has created an urgent demand for high-temperature (HT) resilient energy storage devices with intrinsic safety across mission-critical sectors, particularly in aerospace engineering, oil drilling and extraction, and geophysical exploration operations[1,2]. Compared with organic Li/Na ion batteries, aqueous zinc metal batteries (AZMBs) exhibit nonflammability, high theoretical capacity (820 mAh g^{-1} or 5855 mAh cm^{-3}), and cost-effectiveness, making them highly promising for intrinsically safe electrochemical energy storage systems[3,4]. However, the performance of current AZMBs is hampered by side reactions inherent to aqueous electrolytes, such as hydrogen evolution reaction (HER) and zinc corrosion at the negative electrode, as well as positive electrode material dissolution[5,6]. These issues are kinetically accelerated at elevated temperatures due to enhanced ionic mobility and reaction kinetics[7]. In addition, when the working temperature rises close to the boiling point of water, gas evolution intensifies, leading to battery pack swelling and significantly curtailing the cycle life of AZMBs[8]. Therefore, there is an urgent need to develop long-life AZMBs capable of operating under thermal conditions.

To date, extensive research endeavors have been dedicated to enhancing the electrochemical performance of AZMBs under elevated thermal conditions, involving electrode structure modification[9–11], interface coatings construction[12,13], and HT-resilient electrolytes engineering[5,14,15]. Among these methods, improving the thermal stability of aqueous electrolytes represents a highly effective strategy to optimize the HT performance of AZMBs. Recent advancements in electrolyte formulation demonstrate that gel-based electrolytes[8,16], eutectic electrolytes[15,17], and cosolvent-modified electrolytes[4,18] effectively mitigate the detrimental side reactions in AZMBs, enabling stable cycling performance at elevated temperatures. For instance, Liu

[1]State Key Laboratory of Catalysis, Dalian Institute of Chemical Physics, Chinese Academy of Sciences, Dalian, China. [2]Jiangsu Key Laboratory of Advanced Metallic Materials, School of Materials Science and Engineering, Southeast University, Nanjing, China. [3]These authors contributed equally: Jingxuan Ren, Jie Zhang. ✉e-mail: dongdongwang@dicp.ac.cn; zwchen@dicp.ac.cn

et al. have constructed a multi-component gel electrolyte with multiple advantages of "liquid-like" high conductivity, "gel-like" robust interface, and "solid-like" high Zn^{2+} transfer number, enabling a lifespan of 5000 cycle lifetimes with 91.3% capacity retention at 50 °C[8]. Yan et al. have reported a ternary deep eutectic electrolyte, effectively inhibiting water activity and promoting the interfacial stability of the electrolyte/electrode, thereby enabling long-term operation across a wide temperature range from −20 °C to 70 °C[19]. Han et al. have designed a temperature self-adaptive electrolyte by introducing tetraglyme (TG) with high thermal stability as a cosolvent, forming a carbonate-containing SEI layer conducive to inhibiting HER and electrode corrosion at elevated temperature, leading to an enhanced cycling stability at 75 °C[18]. Previous reports demonstrate that although traditional electrolyte design strategies have made some progress, the performance of AZMBs remains unsatisfactory at high operating temperatures, especially at temperatures close to or even exceeding the boiling point of water. It is necessary to develop an electrolyte strategy to promote the application of AZMBs under thermal conditions.

Herein, we propose an electrolyte strategy of constructing an organic-inorganic-H_2O multiphase aqueous soggy sand electrolyte (MASSE), which endows a high operating temperature of 140 °C for AZMBs. The dual fixation of diethylene glycol solvents and Al_2O_3 nanoparticles greatly limits the activity of free water, as evidenced by molecular dynamics (MD) simulations, Raman, and Fourier transform infrared (FTIR). The multiphase interactions induce water-deficient solvation structures, leading to an improved thermal stability in MASSE, as confirmed by density functional theory (DFT) calculations, extended X-ray absorption fine structure (EXAFS), and in situ temperature Raman. Furthermore, MASSE effectively inhibits water-induced side reactions and facilitates uniform Zn plating/stripping behavior at elevated temperatures, as supported by in situ electrochemical impedance spectroscopy (EIS), differential electrochemical mass spectrometry (DEMS), scanning electron microscopy (SEM), and laser scanning confocal microscope (LSCM). As a result, Zn||PANI full cells exhibit a cycling lifespan of 1700 cycles, an operating temperature of 140 °C, and a high current density of 8 A g^{-1}. Noticeably, MASSE enables the Zn metal pouch cells stable cycling at an HT of 80 °C. This work presents an electrolyte design paradigm enabling AZMBs to operate stably under thermal conditions.

Results

Limited water activity and thermally robust solvation structure in MASSE

The impact of Al_2O_3 particle size on electrolyte stability was first investigated. The zeta potential of MASSE containing different-sized Al_2O_3 particles was utilized to assess the stability between the solid and liquid phases (Supplementary Fig. 1). The absolute value of the zeta potential gradually increases with decreasing Al_2O_3 particle size, indicating the enhanced charge density on the particle surface, which hinders Al_2O_3 sedimentation and phase separation through electrostatic repulsion. Optical images of MASSE further confirm that no observable phase separation occurs when the particle size is reduced to 30 nm, validating the uniformity under actual operating conditions (Supplementary Fig. 2). In addition, the ionic conductivity and viscosity of MASSE electrolytes with different sizes of Al_2O_3 were measured. The viscosity of $Zn(OTf)_2$−DEG and MASSE is greatly increased compared to $Zn(OTf)_2$−H_2O due to the introduction of a large amount of DEG and Al_2O_3 nanoparticles, which leads to enhanced polarization at room temperature (Supplementary Fig. 3a). This phenomenon is closely related to particle size: as particle size decreases, the viscosity of MASSE electrolytes continuously increases, owing to the greater number of surface hydroxyl groups (-OH) (Supplementary Fig. 3b). The ionic conductivity reaches a maximum when 10 nm Al_2O_3 is added, as excessively small particles increase viscosity while overly large particles impede ion migration (Supplementary Fig. 4). Based on a comprehensive consideration of conductivity, viscosity, and stability, subsequent studies selected 10 nm Al_2O_3 as the standard additive component.

Water molecules exhibit three-dimensional hydrogen-bond (HB) networks characterized by diverse O−H−O geometric configurations. Elevated temperatures induce anomalous HB activation in the $Zn(OTf)_2$−H_2O, which manifests as accelerated side reactions. In contrast, our fabricated MASSE demonstrates physical and chemical stability with abundant strong HB formations (Supplementary Fig. 5). To elucidate this phenomenon, DFT calculations were performed. Electron density maps reveal the formation of HB bridges between the components (Fig. 1a and Supplementary Data 1). The H_2O−H_2O HBs in bulk water exhibit a binding energy of −0.314 eV. Introducing DEG or Al_2O_3 creates significantly stronger interactions with a more negative energy difference for H_2O−DEG (−0.364 eV) and H_2O−Al_2O_3 (−0.704 eV). These computational results demonstrate that weak H_2O−H_2O HBs can be effectively disrupted through competitive binding, preferentially forming robust HB networks between additives and water molecules. This synergistic interaction mechanism substantially suppresses water activity by disrupting the original HB framework. The HB populations and interaction strengths in various electrolytes were systematically investigated via MD simulations. Our analysis framework defines HBs geometrically based on two critical parameters: HB angle and HB length, with bond strength exhibiting an inverse correlation with length and direct proportionality to angle. Notably, all simulated systems demonstrate remarkably stable HB configurations, suggesting both thermodynamic and structural convergence of the systems. As illustrated in Fig. 1b, the $Zn(OTf)_2$−H_2O exhibits the highest density of H_2O−H_2O HBs, quantitatively correlating with the maximum water activity observed. In contrast, the $Zn(OTf)_2$−DEG demonstrates significantly reduced HB counts between water molecules, attributable to DEG establishing additional HBs with water species. Notably, in the MASSE, Al_2O_3 introduces strong polar interactions with water, effectively eliminating H_2O−H_2O HB networks while promoting the formation of structurally optimized HB configurations. Figure 1c, d demonstrates a paradoxical phenomenon in the MASSE: While H_2O-H_2O HBs exhibit both elongated bond distances (increasing from ~0.262 nm in $Zn(OTf)_2$−H_2O to 0.277 nm) and contracted bond angles (reducing from 101.8° to 97.4°), these structural modifications correspond to a significant weakening of intermolecular interactions. These results reveal that introducing Al_2O_3 and DEG effectively establishes strong HBs with water molecules (Supplementary Figs. 6–8). This interaction disrupts the original HB networks among water molecules, ultimately leading to a marked suppression of water activity.

The reshaping effect of Al_2O_3 and DEG on the HB networks of H_2O molecules was demonstrated by Raman spectra and FTIR spectra. The stretching vibration of O−H in the range of 3000–4000 cm^{-1} is deconvoluted into two peaks, corresponding to the strong H_2O−H_2O HBs (≈3230 cm^{-1}) and the medium H_2O−H_2O HBs (≈3480 cm^{-1}), respectively (Supplementary Fig. 9). The introduction of Al_2O_3 and DEG greatly attenuates the peak intensity of O−H stretching, revealing a weak water activity. In addition, with the incorporation of Al_2O_3 and DEG, the population of strong HBs decreases by 19% concomitantly with an 81% enhancement in medium HBs, demonstrating strong interaction between the MASSE components and water molecules (Fig. 1e). In the FTIR spectra (Fig. 1f), the O−H stretching vibration of H_2O in electrolytes within the range of 3000–3800 cm^{-1} is deconvoluted into three peaks, assigned to "network water" (NW, 3205 cm^{-1}), "intermediate water" (IW, 3433 cm^{-1}), and "multimer water" (MW, 3560 cm^{-1}). The NW depicts water molecules with strong HBs, while the MW reveals a weak HB and a poor link to the surrounding water[20]. The impact of the MASSE components on the HB network can be quantitatively analyzed by comparing the areal ratios of NW, IW, and MW, as displayed in Fig. 1g. The MASSE exhibits the highest proportion of MW

https://doi.org/10.1038/s41467-025-67020-z

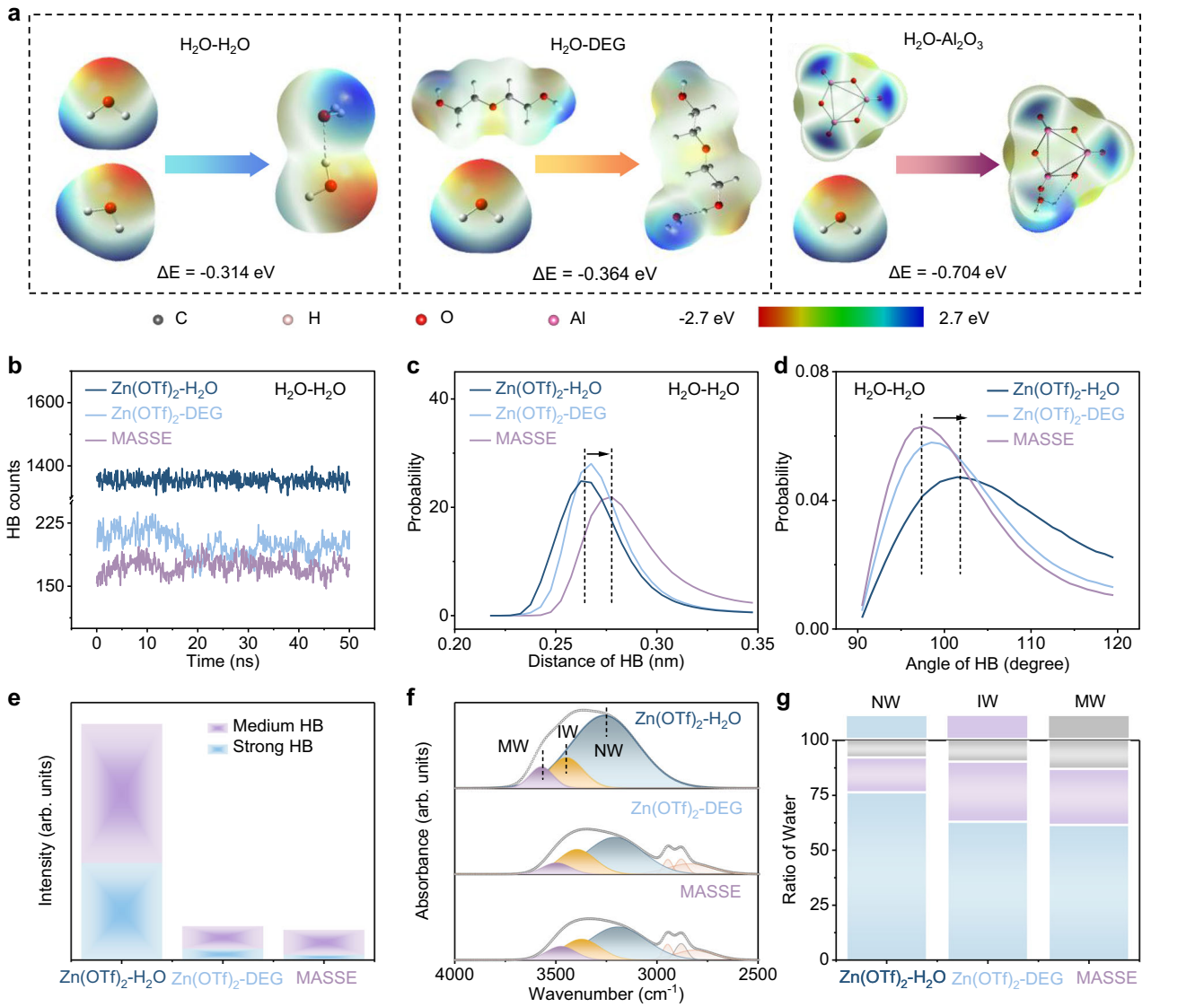

Fig. 1 | The inhibition of water activity in MASSE. a Electron density maps and energy difference of hydrogen-bond (HB) complexes between H_2O–H_2O, H_2O–DEG, and H_2O–Al_2O_3; MD simulation results of the H_2O–H_2O HBs in different electrolytes: **b** counts, **c** distances, **d** angles of the HBs; **e** The intensity of strong H_2O–H_2O HBs and medium H_2O–H_2O HBs in different electrolytes, obtained by Raman spectra; **f** The FTIR spectra of O–H stretching vibration of water molecules in different electrolytes; **g** Comparison of the areal ratios of network water (NW), intermediate water (IW), and multimer water (MW) in different electrolytes.

and the lowest proportion of NW component among all electrolytes, which indicates a drastically decreased water activity and, consequently, an improved thermal stability.

The HT performance of AZMBs is fundamentally governed by the thermal robustness of the solvation structures in the electrolyte. Structural instability within these solvation complexes can trigger a cascade of detrimental electrochemical processes, including electrolyte decomposition, interfacial impedance escalation, and uncontrollable side reactions, ultimately leading to thermal runaway scenarios[21]. MD simulations were conducted to investigate the Zn^{2+} solvation shells at 80 °C (Supplementary Data 2–4). As shown in Fig. 2a–c, 3D snapshots from the MD simulations demonstrate homogeneous spatial distribution of all constituent species, especially Al_2O_3. To quantify the local environment around Zn^{2+}, the radial distribution function (RDF) with respect to Zn^{2+} and the coordination number (CN) were calculated (Supplementary Table 1). Figure 2d illustrates that H_2O and OTf^- in the solvation sheath are located at 1.92 Å and 1.86 Å away from Zn^{2+}, with an average CN of 5.05 and 0.95 for Zn^{2+}, which generates H_2O-rich Zn^{2+} solvates for $Zn(OTf)_2$–H_2O. In the $Zn(OTf)_2$–DEG, the CN of H_2O decreases to 0.86, and DEG appears at 1.9 Å away from Zn^{2+} with an average CN of 3.75 (Fig. 2e). Notably, as evident from Fig. 2f, Al_2O_3 species with a CN of 0.68 exhibit preferential spatial association with Zn^{2+}. The emergence of the Al_2O_3 RDF peak stems from the DEG-induced electrostatic interaction, which effectively bridges the interfacial gap between Zn^{2+} and Al_2O_3, enabling the periodic arrangement of Al_2O_3 within the Zn^{2+} solvation shells, thereby generating specific spectral signals characteristic of coordination (Supplementary Fig. 10). The same phenomena are also observed in SiO_2 inorganics[22]. The primary solvation shell of Zn^{2+} exhibits a marginal depletion of OTf^- ligands (CN = 1.21) alongside a significant displacement of water molecules (CN = 0.61), manifesting a water-deficient solvation structure. The representative Zn^{2+} solvation structures and their corresponding percentages were extracted, as shown in Supplementary Fig. 11 and Supplementary Tables 2–4. We identify the particular solvation structures in different electrolytes for subsequent discussion.

X-ray absorption fine structure analysis was carried out to investigate the solvation sheath of Zn^{2+}. The Zn K-edge X-ray absorption near-edge structure (XANES) spectra of different electrolytes are displayed in Fig. 2g.

https://doi.org/10.1038/s41467-025-67020-z

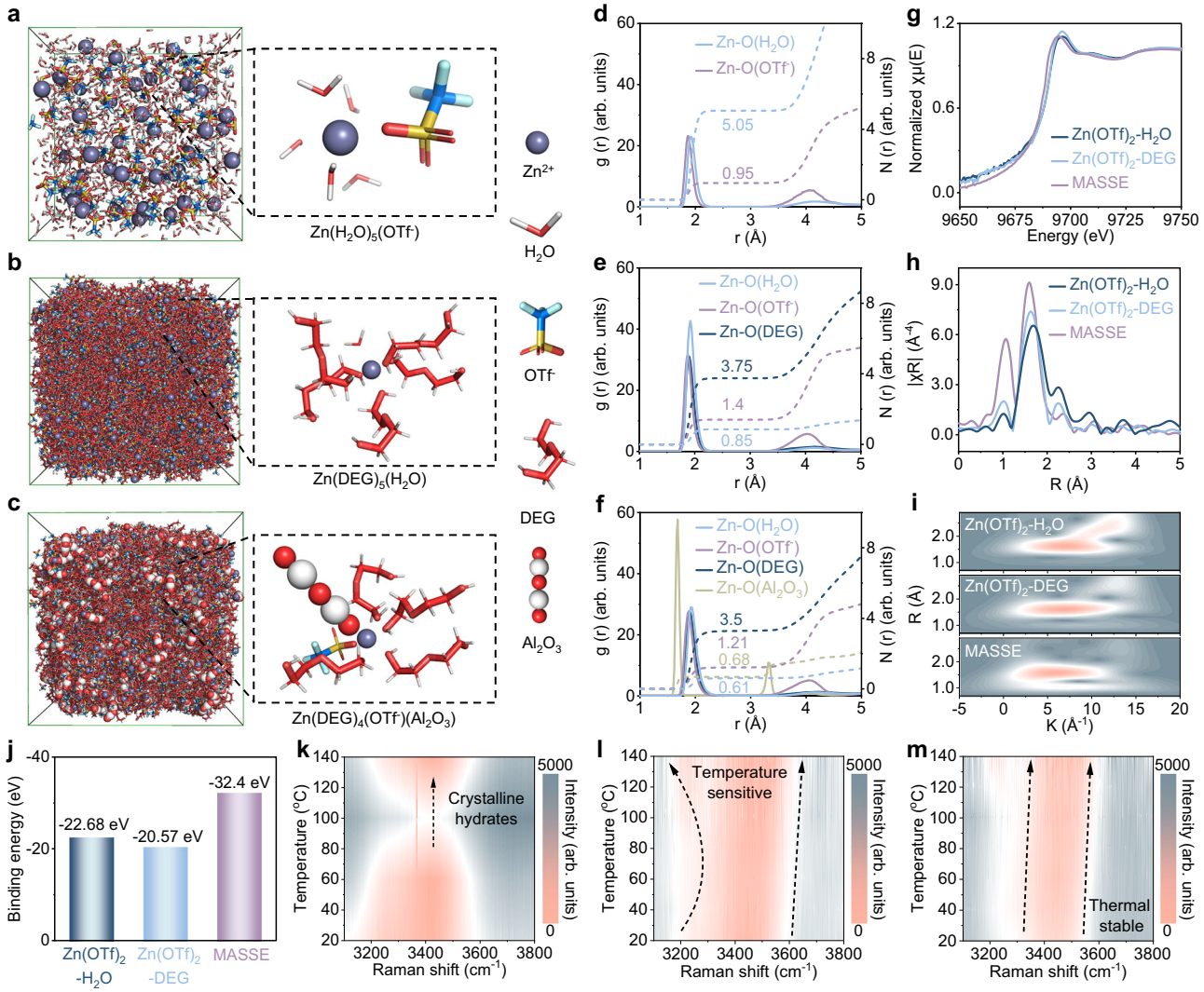

Fig. 2 | Thermally robust solvation structures of MASSE. 3D snapshots and representative solvation structures collected from MD simulations in **a** $Zn(OTf)_2$–H_2O, **b** $Zn(OTf)_2$–DEG and **c** MASSE; the radial distribution functions and coordination number of Zn^{2+} in **d** $Zn(OTf)_2$–H_2O, **e** $Zn(OTf)_2$–DEG, **f** MASSE; **g** the normalized Zn K-edge XANES spectra of different electrolytes; **h** Fourier transformations of Zn K-edge EXAFS spectra of different electrolytes; **i** wavelet transform images of the EXAFS spectra of different electrolytes; **j** the binding energies of the representative solvation structures in different electrolytes; in situ Raman spectra of O–H stretching in **k** $Zn(OTf)_2$–H_2O, **l** $Zn(OTf)_2$–DEG, **m** MASSE at different temperatures.

The near-edge absorption energy of MASSE shifts to lower regions, indicative of enhanced electron donation from Al_2O_3 ligands, which effectively lowers the Zn^{2+} oxidation state[23]. As illustrated in Fig. 2h, the contraction of the Zn–O bond length observed in MASSE correlates with enhanced ligand coordination stability, suggesting a more robust solvation network[24]. Additionally, the wavelet-transformed EXAFS was carried out to further elucidate the local solvation structure of Zn^{2+}. The pink regions refer to the locations where the peaks of R-space and k-space coincide. In three electrolytes, these regions are located at low k and R values, reflecting similar Zn–O coordination, whether it involves the Zn–H_2O, Zn–DEG, Zn–OTf^-, or Zn–Al_2O_3 (Fig. 2i). These findings are consistent with FTIR and Raman spectra (Supplementary Figs. 12 and 13). The dominant solvation configuration ($Zn(H_2O)_5(OTf^-)_1$) in $Zn(OTf)_2$–H_2O was computationally modeled. The incorporation of Al_2O_3 induces structural reorganization. This leads to the replacement of the primary solvation structure, from $Zn(H_2O)_1(DEG)_5$ in the $Zn(OTf)_2$–DEG electrolyte to $Zn(OTf^-)_1(DEG)_4(Al_2O_3)_1$ in MASSE. Notably, three other solvation configurations remain consistent throughout this process. The binding energies corresponding to these three characteristic solvation structures were calculated (Fig. 2j and Supplementary Fig. 14) (Supplementary Data 1). The distinctive solvation structure in the MASSE exhibits the highest binding energy (−32.4 eV) compared to the $Zn(OTf)_2$–H_2O (−22.68 eV) and the $Zn(OTf)_2$–DEG (−20.57 eV), demonstrating enhanced structural stability and preventing structural damage at elevated temperatures.

The configurational stability of electrolytes was systematically investigated using in situ Raman spectra under different temperatures. The $Zn(OTf)_2$–H_2O demonstrates restricted thermal stability, as evidenced by the initiation of $Zn(OTf)_2$ crystallite precipitation at 80 °C, owing to salt precipitation caused by electrolyte evaporation (Fig. 2k)[20]. Figure 2l demonstrates a thermo-responsive behavior of $Zn(OTf)_2$–DEG through O–H stretching band broadening as temperature rises from 20 to 140 °C. For MASSE, the O–H stretching intensity increases between 20 and 60 °C and then remains stable without obvious enhancement as the heating temperature increases to 140 °C. In addition, the O–H band in the MASSE electrolyte maintains much lower intensity compared to the $Zn(OTf)_2$–H_2O and $Zn(OTf)_2$–DEG electrolyte, attributable to Al_2O_3-induced ligand cross-linking that stabilizes the solvation network against thermal fluctuations (Fig. 2m). Thermogravimetry curves of different electrolytes were employed in Supplementary Fig. 15. The MASSE possesses enhanced thermal

https://doi.org/10.1038/s41467-025-67020-z

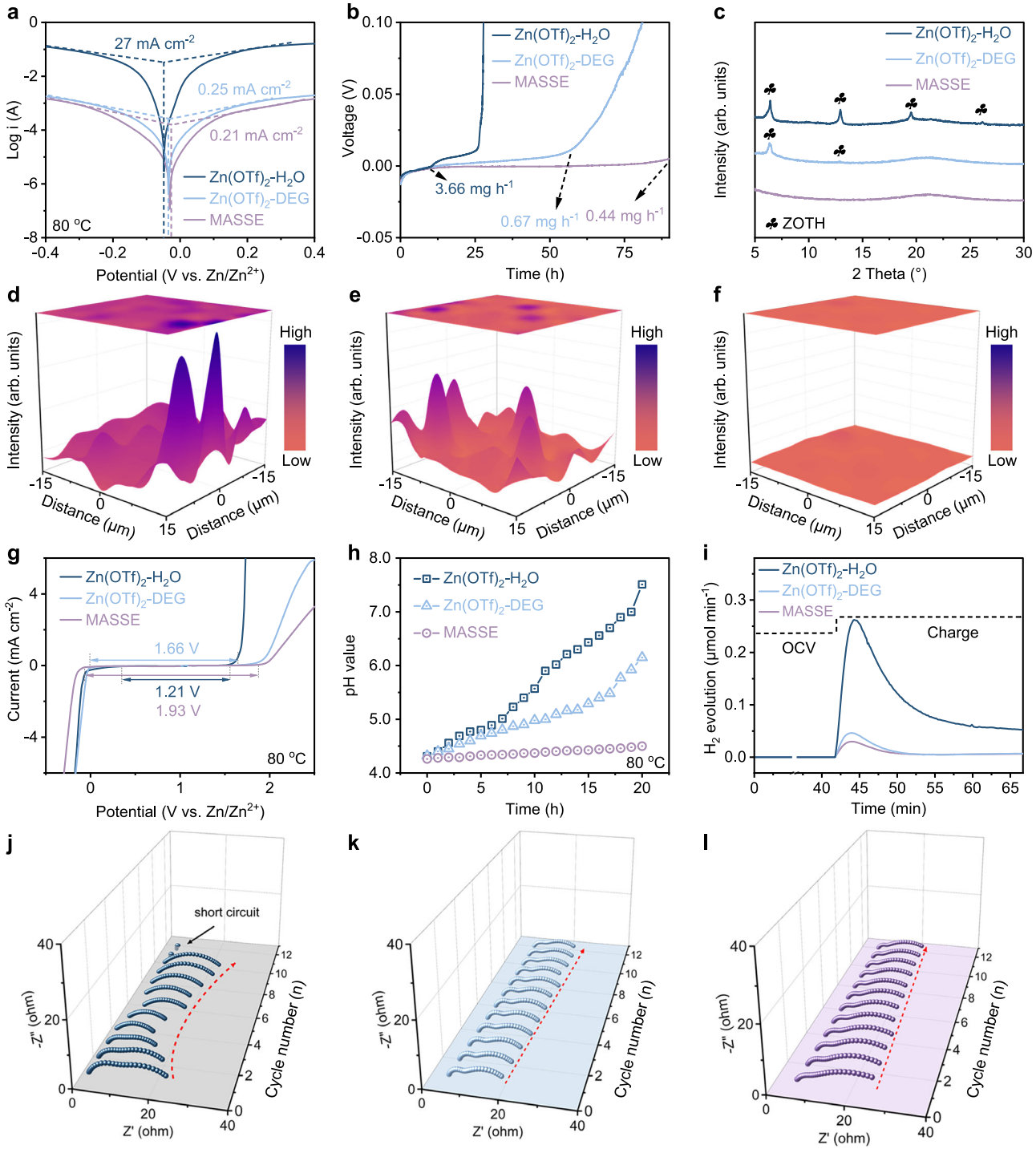

Fig. 3 | The inhibited side reactions of MASSE at elevated temperature. a The Tafel plots of different electrolytes at 80 °C. **b** Voltage-time profiles for Zn@Cu electrodes immersed in different electrolytes at 80 °C. **c** $Zn_{x+y}(OTf)_{2y}(OH)_{2x}$ (ZOTH) peaks in Zn negative electrode XRD patterns after 50 cycles (80 °C). 3D Raman mapping on the surfaces of cycled Zn negative electrodes in **d** $Zn(OTf)_2$–H_2O, **e** $Zn(OTf)_2$–DEG, **f** MASSE. **g** LSV curves of different electrolytes at 80 °C. **h** In situ pH value in different electrolytes; **i** DEMS profiles of H_2 evolution in Zn||Zn symmetric cells containing different electrolytes at 80 °C. In situ EIS curves of Zn||Zn cells during cycling in **j** $Zn(OTf)_2$–H_2O, **k** $Zn(OTf)_2$–DEG, **l** MASSE.

stability, retaining 99.1% of its weight at 150 °C, compared to 82.1% for $Zn(OTf)_2$–DEG and 43.7% for $Zn(OTf)_2$– H_2O, which is consistent with the DFT calculations.

Suppressing parasitic reactions and Zn dendrites under elevated temperature

The thermally robust solvation structure in MASSE plays a crucial inhibitory role in the rampant parasitic reactions at HT. As shown in Fig. 3a, the corrosion behavior of the Zn negative electrode in different electrolytes was compared by Tafel plots. Compared to the $Zn(OTf)_2$–H_2O and $Zn(OTf)_2$–DEG, the MASSE exhibits the smallest corrosion current and the highest corrosion potential at 80 °C. As displayed in Fig. 3b, the potential of the Zn@Cu electrode grows dramatically once the electrolyte corrodes all of the metallic Zn[14]. The corrosion rate of Zn in the MASSE is 0.41 mg h^{-1}, much slower than that in the $Zn(OTf)_2$–H_2O (3.66 mg h^{-1}) and in the $Zn(OTf)_2$–DEG

(0.67 mg h^{-1}), indicating a lower Zn corrosion reaction in MASSE. The protection of the Zn negative electrode from side reactions was also verified through X-ray diffraction (XRD) patterns. As shown in Fig. 3c, there are obvious characteristic peaks related to zinc triflate hydroxide hydrate ($Zn_{x+y}(OTf)_{2y}(OH)_{2x}$, ZOTH) in the $Zn(OTf)_2$–H_2O and $Zn(OTf)_2$–DEG after 50 cycles. In contrast, the intensity of these by-products on the cycled Zn negative electrode in MASSE is significantly diminished. Subsequently, 3D Raman mapping (30 × 30 area) was used to spatially resolve ZOTH by-products distribution on cycled Zn negative electrodes. Characteristic strong peaks emerge in $Zn(OTf)_2$–H_2O and $Zn(OTf)_2$–DEG, whereas MASSE displays a complete absence of these signatures, confirming effective suppression of parasitic reactions (Fig. 3d–f and Supplementary Fig. 16)[25,26].

Linear sweep voltammetry (LSV) testing exhibits that MASSE demonstrates the largest electrochemical window (1.81 V < 2.24 V < 2.68 V) among all electrolytes at 25 °C (Supplementary Fig. 17). At an elevated temperature of 80 °C, all electrolytes exhibit marginally narrowed electrochemical windows, attributable to aggravated side reactions. Nonetheless, MASSE maintains the widest electrochemical window (1.93 V), exceeding that of both $Zn(OTf)_2$–H_2O (1.21 V) and $Zn(OTf)_2$–DEG (1.66 V) (Fig. 3g). In situ pH monitoring over 20 h exhibits that the pH value of $Zn(OTf)_2$–H_2O increases rapidly throughout the entire cycle. This rise is caused by severe HER, which leads to higher local pH values and exacerbates the formation of ZOTH by-products at both 25 °C and 80 °C (Fig. 3h and Supplementary Fig. 18). The pH value of the $Zn(OTf)_2$–DEG shows a slight easing trend but still increases. In sharp contrast, the pH values of MASSE remain relatively constant under the same conditions, indicating the substantial inhibitory effect on HER. The suppression of HER enabled by MASSE is further investigated using in situ DEMS. Figure 3i and Supplementary Fig. 19 present the quantitative DEMS results of H_2 evolution during the OCP and charge process at 25 °C and 80 °C. Significantly reduced H_2 evolution is observed at the Zn negative electrode surface utilizing the MASSE electrolyte, under room-temperature and elevated-temperature conditions. Furthermore, in situ EIS was tested to visually reflect the inhibitory effect of MASSE on parasitic reactions at 80 °C (Supplementary Fig. 20). As shown in Fig. 3j and Supplementary Fig. 21, $Zn(OTf)_2$–H_2O experiences a short circuit after 12 cycles, attributable to progressive electrolyte depletion and by-products accumulation at HT. The $Zn(OTf)_2$–DEG displays escalating electrochemical impedance during the cycling process, likely stemming from insulating deposit formation under HT (Fig. 3k and Supplementary Fig. 22). Conversely, MASSE demonstrates progressively diminishing interfacial impedance accompanied by marginally attenuated voltage hysteresis throughout cycling (Fig. 3l and Supplementary Fig. 23). This is attributable to reinforced ligand coordination frameworks. MASSE effectively inhibits the water activity at HT. Meanwhile, the effective mitigation of parasitic reactions in MASSE is also attributed to the stable and ZnF_2-enriched electrode/electrolyte interfaces (Supplementary Figs. 24–27).

The Zn morphology of different electrolytes at room temperature is examined by SEM. As shown in Fig. 4a, d, g, Zn deposited in MASSE exhibits a more uniform and dendrite-free morphology compared to that in $Zn(OTf)_2$–H_2O and $Zn(OTf)_2$–DEG. The morphology of the Zn negative electrode of different electrolytes was characterized at 80 °C. After Zn deposition, randomly oriented and porous clusters of Zn dendrites are observed in $Zn(OTf)_2$–H_2O and $Zn(OTf)_2$–DEG (Fig. 4b, e). However, the surface of the Zn negative electrode in MASSE is densely packed after Zn deposition (Fig. 4h). After 50 cycles, large amounts of randomly-oriented flakes and dendrites are formed on the surface of Zn negative electrode in $Zn(OTf)_2$–H_2O and $Zn(OTf)_2$–DEG (Fig. 4c, f), while the surface of the Zn negative electrode in MASSE is compact and relatively smooth (Fig. 4i). LSCM images exhibit a high roughness with large protrusions in the $Zn(OTf)_2$–H_2O (Fig. 4j). Despite exhibiting marginal enhancement in electrodeposition microstructure, the $Zn(OTf)_2$–DEG retains irregular surface topography with pronounced defects (Fig. 4k). MASSE preserves a planar morphology with a low surface roughness at elevated temperature (Fig. 4l). These results demonstrate that a dendrite-suppression plating morphology is obtained in the MASSE at HT, which is attributed to thermally robust solvation structures of MASSE. Figure 4m–o systematically elucidates the underlying mechanisms of the HT stability of the MASSE, integrating the aforementioned experimental and computational insights. Ligand coordination reinforcement results in the formation of a temperature-insensitive solvation structure. The optimized HB configurations in the MASSE lead to a low water activity. Therefore, such advantages effectively inhibit parasitic reactions (HER, Zn corrosion) caused by excessive free water, and promote a uniform Zn deposition at elevated temperature.

Enhanced high-temperature performance in MASSE

Asymmetric Zn||Cu cells were assembled to evaluate the Zn plating/striping reversibility. The applied current density influences the measured CE, and high current densities can obscure the impact of HER. Therefore, a low current density of 1 mA cm^{-2} was used for testing at 80 °C. As shown in Fig. 5a, half-cells using the $Zn(OTf)_2$–H_2O show drastic fluctuations and rapid decay in CE, lasting only 50 cycles due to severe parasitic reactions and the growth of Zn dendrites. For $Zn(OTf)_2$–DEG, Zn||Cu cell exhibits a low average CE of 95.64% and a short cycle life. In contrast, Zn||Cu cell using MASSE exhibits a high average CE of 98.60% and a significantly extended lifespan of 1200 cycles. When the current density increases to 2 mA cm^{-2}, enhanced cycle life and CE are also obtained in MASSE (Supplementary Fig. 28). The Zn plating/stripping behavior was also analyzed by symmetric Zn||Zn cells. As shown in Fig. 5b, the Zn||Zn cells with MASSE exhibit a lifespan of 600 h, much longer than that of $Zn(OTf)_2$–H_2O and $Zn(OTf)_2$–DEG. Elevated-temperature electrochemical cycling presents intensified hurdles compared to ambient-condition cell operation, primarily due to accelerated interfacial degradation and thermal-driven electrolyte decomposition. MASSE with 10% Al_2O_3 shows the optimal cycling performance at 80 °C (Supplementary Fig. 29). At a low current density of 1 mA cm^{-2}, cells with $Zn(OTf)_2$–H_2O undergo a rapid short circuit at 9 h at 80 °C. The cells with $Zn(OTf)_2$–DEG also experience a short circuit at 920 h. The Zn||Zn symmetric cells using MASSE demonstrate stable cycling for at least 1120 h at 80 °C (Supplementary Figs. 30 and 31). Similarly, at 2 mA cm^{-2} and 1 mAh cm^{-2}, symmetric cells using the MASSE exhibit a stable cycling for over 900 h without significant fluctuations of overpotential, while cells with the $Zn(OTf)_2$–H_2O and $Zn(OTf)_2$–DEG exhibit a short lifespan at 80 °C (Fig. 5c and Supplementary Fig. 32). When the current density and the reversible capacity increase to 4 mA cm^{-2} and 2 mAh cm^{-2}, the Zn||Zn cells using MASSE manifest a stable cycling for 140 h with a lower overpotential around 260 mV (Supplementary Fig. 33). Unfortunately, the cells using $Zn(OTf)_2$–H_2O and $Zn(OTf)_2$–DEG experience a rapid increase of polarization voltage and a quick short circuit (14 h and 45 h). To verify the advantages of the MASSE under a high current density, the rate performance of symmetric cells was measured at 80 °C (Fig. 5d). Zn||Zn cells with $Zn(OTf)_2$–H_2O fail rapidly at 2 mA cm^{-2}, while those with $Zn(OTf)_2$–DEG exhibit a large overpotential at 4 mA cm^{-2}. The symmetric cells with MASSE exhibit a stable voltage profile and low voltage hysteresis even at a high current density of 8 mA cm^{-2} at 80 °C. The cycling performance of Zn||Zn and Zn||Cu cells is further evaluated under practical conditions with a depth-of-discharge (DOD) of 50%, followed by characterization of the post-cycled negative electrodes (Supplementary Figs. 34 and 35). The significantly enhanced performance of MASSE under high current density is attributed to the rapid migration of Zn^{2+} (Supplementary Figs. 36 and 37 and Supplementary Table 5)[27,28]. Even at a boiling point temperature of 100 °C, the Zn||Zn cells using MASSE demonstrate a stable cycling over 130 h (Fig. 5e). More intuitively, the wide temperature tolerance under a more stringent external environment, ranging from 25 to 140 °C, was investigated. Zn||Zn cells using MASSE

https://doi.org/10.1038/s41467-025-67020-z

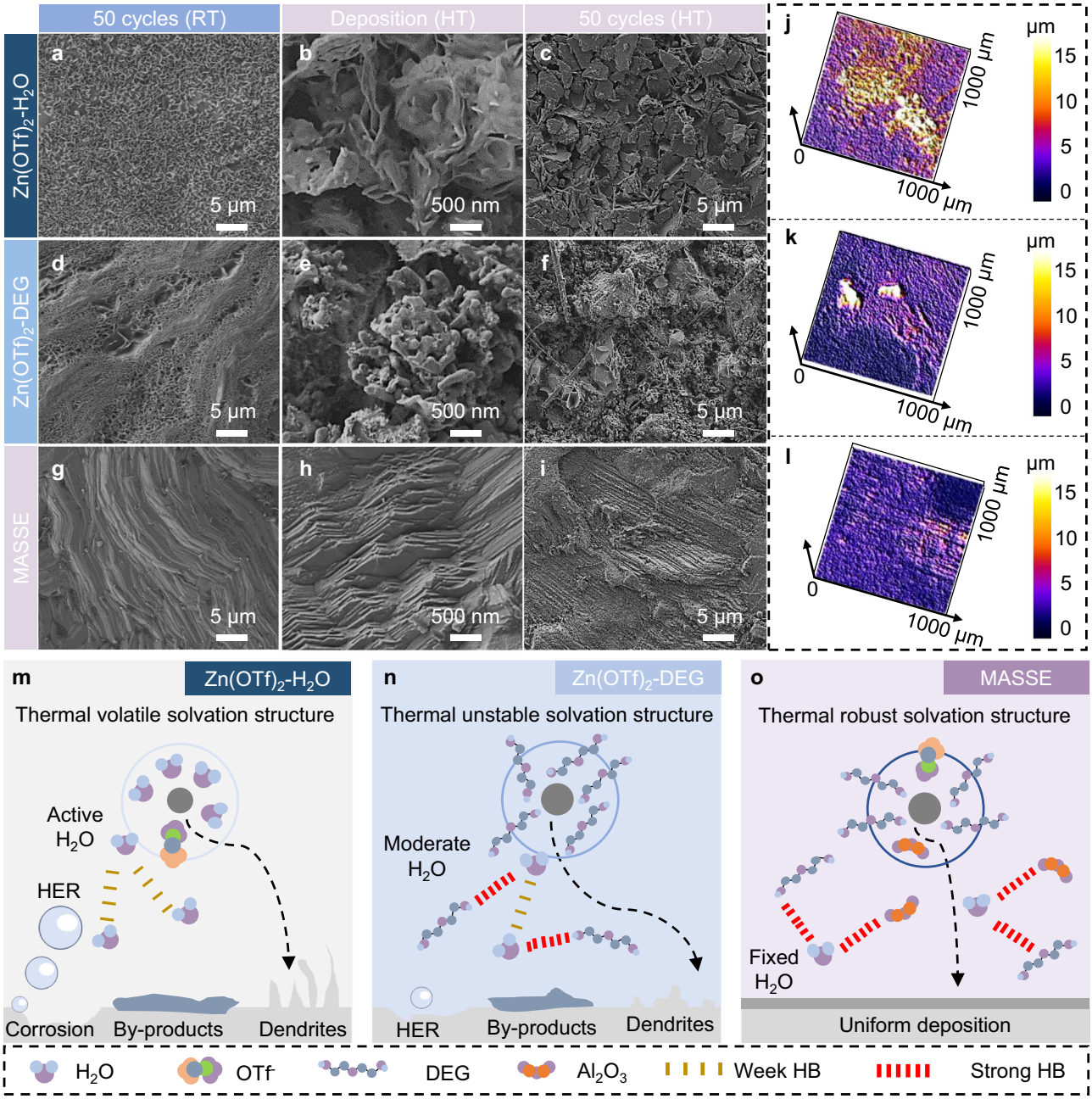

Fig. 4 | Suppressing Zn dendrites in MASSE at elevated temperature. SEM images of Zn negative electrodes after 50 cycles at room temperature (RT) in **a** $Zn(OTf)_2$–H_2O, **d** $Zn(OTf)_2$–DEG, and **g** MASSE. Zn deposition morphology at 80 °C in **b** $Zn(OTf)_2$–H_2O, **e** $Zn(OTf)_2$–DEG, and **h** MASSE; SEM images of Zn negative electrode after 50 cycles at 80 °C in **c** $Zn(OTf)_2$–H_2O, **f** $Zn(OTf)_2$–DEG, and **i** MASSE. LSCM images of the Zn negative electrode after 50 cycles at 80 °C in **j** $Zn(OTf)_2$–H_2O, **k** $Zn(OTf)_2$–DEG, and **l** MASSE; **m**–**o** Schematic illustration about the underlying mechanism of enhanced high temperature (HT) performance in MASSE.

exhibit normal voltage curves even at operating temperatures of 140 °C without short circuiting, suggesting high thermal stability of MASSE (Fig. 5f). In contrast, the symmetrical cells with $Zn(OTf)_2$–H_2O and $Zn(OTf)_2$–DEG fail at 100 °C and 120 °C, respectively, demonstrating inadequate temperature tolerance under elevated thermal conditions (Supplementary Fig. 38). We compared the reported cycle life of Zn||Zn cells at elevated temperatures. Notably, this work demonstrates competitive cycling performance at high current density, large areal capacity, and a high operating temperature (Fig. 5g and Supplementary Table 6). Large-scale Zn||Zn pouch cells with an area of 25 cm^2 were assembled to exemplify the practical application feasibility of MASSE at HT. The increase of the negative electrode area usually intensifies the uneven nucleation of Zn^{2+}, dendrite growth, and by-products generation, specifically under thermal conditions. Yet, benefitting from the thermally robust Zn^{2+} solvation structure and confined water reactivity in MASSE, Zn||Zn pouch cells exhibit stable cycling for over 400 h at 80 °C, much longer than that in $Zn(OTf)_2$–H_2O and $Zn(OTf)_2$–DEG.

To evaluate the practical applications of the MASSE, polyaniline (PANI) was employed as a positive electrode to pair with the Zn negative electrode for full cell testing. Firstly, the performance of the MASSE-assembled full cells was tested at room temperature to verify their universality under ambient conditions. The Zn||PANI full cells employing MASSE demonstrate cycling stability of 2000 cycles, which

https://doi.org/10.1038/s41467-025-67020-z

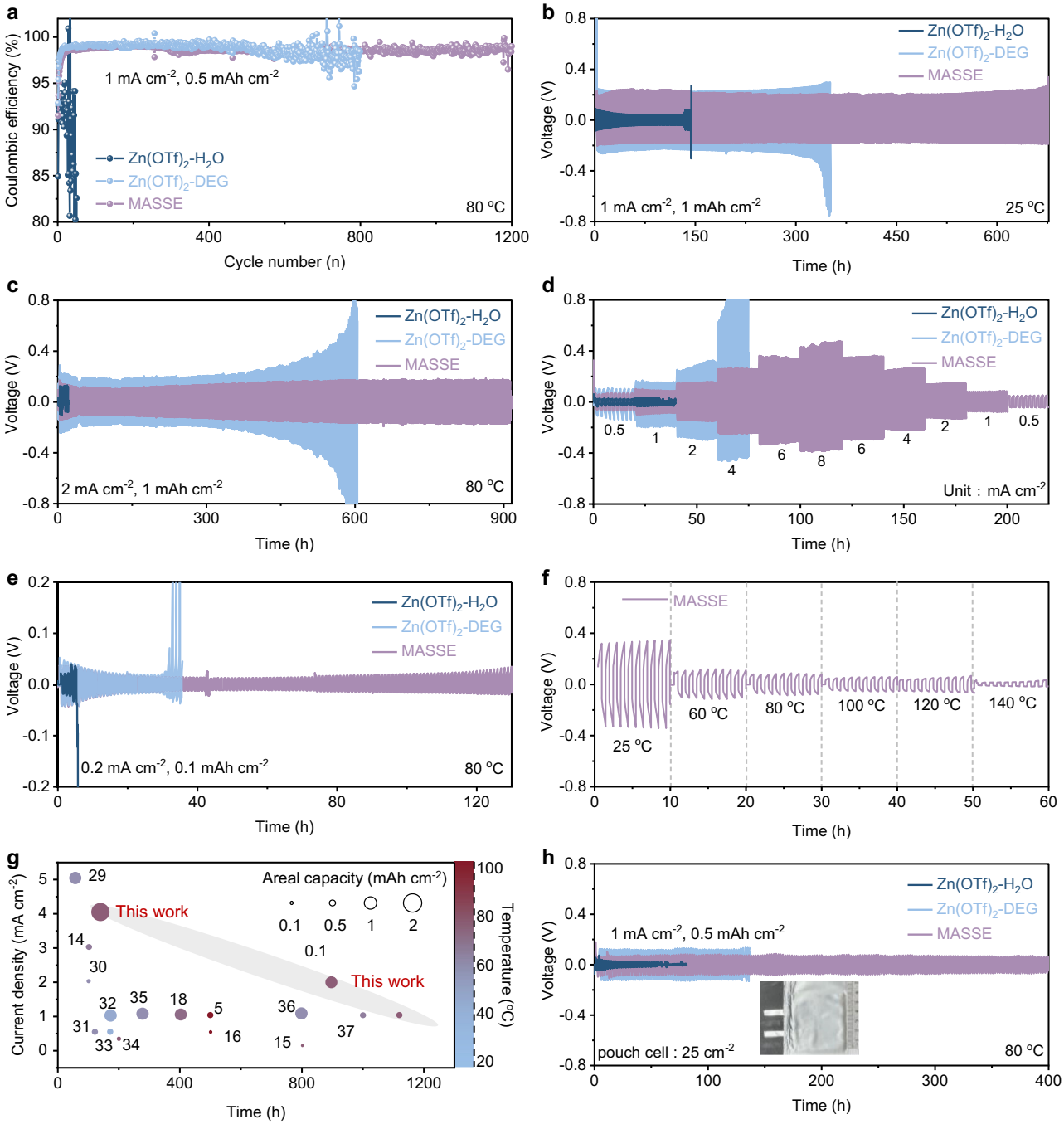

Fig. 5 | Electrochemical performance of half-cells at elevated temperature. **a** Cycling performance of Zn||Cu cells using different electrolytes at current density of 1 mA cm^{-2} under 80 °C; **b** cycling performance of Zn||Zn cells using different electrolytes under 1 mA cm^{-2} and 1 mAh cm^{-2} at 25 °C; **c** cycling performance of Zn||Zn cells using different electrolytes under 2 mA cm^{-2} and 1 mAh cm^{-2}; **d** rate performance of Zn||Zn cells with different electrolytes at 80 °C; **e** cycling performance of Zn||Zn cells using different electrolytes under 0.2 mA cm^{-2} and 0.1 mAh cm^{-2} at 100 °C; **f** cycling performance of Zn||Zn cells using MASSE at different temperatures; **g** comparison of the cycling performance of Zn||Zn cells with previous reports at elevated temperatures[5,14–16,18,29–37] (The source of the literature data shown in this figure can be found in Supplementary Table 6). **h** Cycling performance of Zn||Zn pouch cells using different electrolytes at 80 °C.

far surpasses that of $Zn(OTf)_2$–H_2O and $Zn(OTf)_2$–DEG (Fig. 6a). At an elevated temperature of 80 °C, Zn||PANI full cells with MASSE maintain a cycle life of 1700 cycles, substantially longer than that achieved with $Zn(OTf)_2$–H_2O or $Zn(OTf)_2$–DEG electrolytes (Fig. 6b and Supplementary Fig. 39). Furthermore, full cells with MASSE exhibit higher CE and greater reversibility during charging and discharging than those with $Zn(OTf)_2$–H_2O or $Zn(OTf)_2$–DEG, due to inhibited side reactions at HT. The rate performance of Zn||PANI full cells with different electrolytes was tested at 80 °C (Fig. 6c). The MASSE-based full cells show rate performance at a current density range from 0.8 to 8.0 A g^{-1}, with capacities ranging from 126 to 65 mAh g^{-1}. When the current density is returned to 0.5 A g^{-1}, the specific capacity remains stable, demonstrating performance better than that of cells with $Zn(OTf)_2$–H_2O or $Zn(OTf)_2$–DEG electrolytes (Supplementary Fig. 40). The enhanced performance difference under high current can be attributed to the rapid migration of Zn^{2+} in MASSE. The cycle life of MASSE was further evaluated in the full cells of Zn||PANI under more stringent testing conditions with N/P of 2 (50% DOD) (Supplementary Fig. 41). The

https://doi.org/10.1038/s41467-025-67020-z

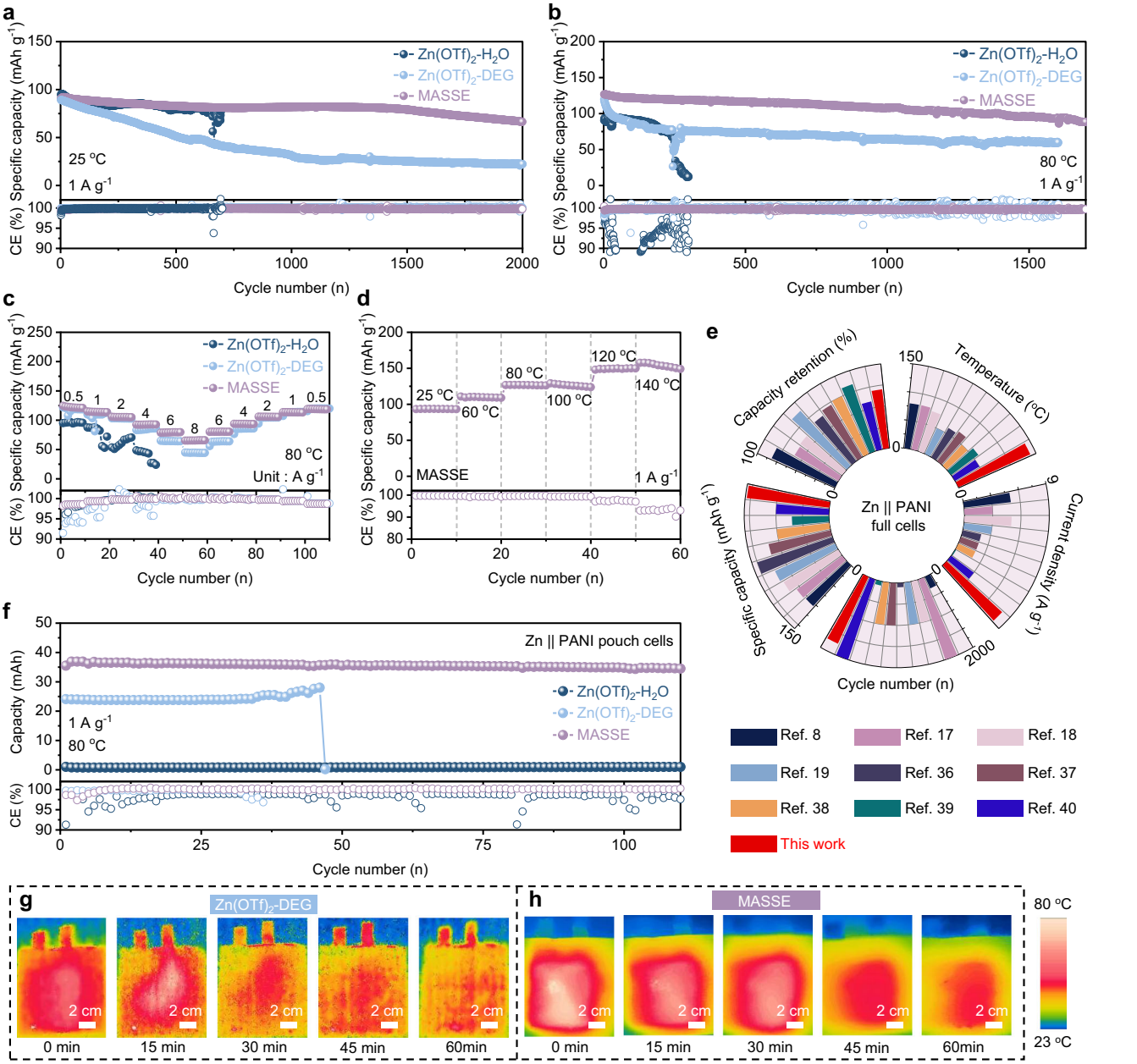

Fig. 6 | Enhanced HT performance of full cells using MASSE. Cycling performance and CE of Zn||PANI full cells using different electrolytes under **a** room temperature and **b** 80 °C. **c** rate performance and CE of Zn||PANI full cells with different electrolytes at 80 °C; **d** electrochemical performance of Zn||PANI full cells using MASSE at various temperatures. **e** The overall comparison of full cells' performance between MASSE and previous reports[8,17–19,36–40] (The source of the literature data shown in this figure can be found in Supplementary Table 7). **f** Cycling performance and CE of Zn||PANI pouch cells with different electrolytes. Thermal imaging of the pouch cells charged at 1 A g^{-1} for 1 h in **g** $Zn(OTf)_2$–DEG and **h** MASSE.

favorable performance prompts an evaluation of the electrochemical performance at higher working temperatures. As shown in Fig. 6d, Zn||PANI full cells display a stable charge and discharge process with a gradually increasing specific capacity as the temperature increases from 25 to 140 °C. Even at an HT of 140 °C, the full cell still operates normally with a high specific capacity of 157 mAh g^{-1}. Moreover, the full cells using MASSE still maintain stable cycling under high current density of a 8 A g^{-1} and a high working temperature of 140 °C (Supplementary Fig. 42). As summarized in Fig. 6e, Zn||PANI full cells utilizing MASSE demonstrate competitive performance against some recent relevant reports, which is attributed to their long cycle life, high-rate capability, and excellent HT tolerance (Supplementary Table 7). This comparison underscores the great advantages of MASSE for HT AZMBs.

HT full cells evaluations remain predominantly limited to the coin cells due to accelerated parasitic reactions (e.g., Zn corrosion, HER, SEI dissolution) in the pouch cells under elevated temperature, which induces catastrophic capacity fade in scaled systems. Therefore, the feasibility of the MASSE was first evaluated in the pouch cells. As displayed in Fig. 6f, a large-sized pouch cell using MASSE delivers a total capacity of 37 mAh with stable cycling over 175 cycles at 80 °C. Oppositely, the pouch cells using the $Zn(OTf)_2$–H_2O and $Zn(OTf)_2$–DEG release low capacity with rapid capacity decay. Furthermore, the MASSE-assembled pouch cells can power a lamp (Supplementary Fig. 43), which shows great promise in practical applications. Considering the intimate connection between intrinsic reactions and thermal effects, the heat distribution of pouch cells during actual operation has been investigated by infrared thermal

imaging. Initially, the pouch cells with different electrolytes were cycled three times at a current density of 1 A g^{-1} and a temperature of 80 °C, before being returned to room temperature for thermal monitoring. During the static period, the temperature varies greatly in different regions in the $Zn(OTf)_2$–H_2O and $Zn(OTf)_2$–DEG (Supplementary Fig. 44 and Fig. 6g). A few areas have a concentrated HT, indicating that these are the sites of intensive side reactions, e.g., large-scale HER and corrosion. In contrast, the temperature of pouch cells using MASSE is uniformly distributed, which demonstrates the uniform reactions at HT (Fig. 6h). These results further demonstrate that MASSE effectively inhibits side reactions at elevated temperatures, even in the large-sized pouch cells. To verify the universality of the proposed MASSE design strategy, two parallel investigations were conducted. First, DEG solvent was replaced with various representative organic solvents (alcohols, sulfones, and esters) to systematically evaluate the HT electrochemical performance of the corresponding MASSE systems (Supplementary Fig. 45). In addition, the MASSE electrolyte was extended and applied to Zn||NVO full cell systems beyond the Zn||PANI system (Supplementary Fig. 46). The results demonstrate that the MASSE electrolyte developed in this study is not only compatible with diverse solvent systems but also adaptable to different electrode material systems, achieving long-term cycling stability under elevated temperatures in all cases.

Discussion

In summary, a thermally robust MASSE is designed for enhancing the HT performance of AZMBs. Detailed experimental characterizations and theoretical calculations reveal that optimized HBs configurations and water-deficient solvation structures in MASSE effectively eliminate parasitic reactions and inspire a uniform Zn deposition at elevated temperatures. Benefiting from these advantages, MASSE enables Zn metal full cells to achieve a long lifespan of 1700 cycles, a high operating temperature of 140 °C, and a high current density of 8 A g^{-1}. Even in Zn metal pouch cells, the benefits provided by this electrolyte are still pronounced. This work opens up an electrolyte design paradigm that enables AZMBs to operate stably under thermal conditions.

Methods

Materials

Zinc trifluoromethylsulfonate ($Zn(OTf)_2$, AR ≥ 99%) was purchased from Sigma-Aldrich. Diethylene glycol (DEG, AR ≥ 99%), alumina (Al_2O_3, 10 nm, AR ≥ 99.8%), N-Methyl-2-pyrrolidone (NMP, AR ≥ 99.5%), and polyaniline (PANI) were purchased from Aldrich. Ketjen Black, Polytetrafluoroethylene (PTFE), Zinc foil (99.9%), stainless-steel mesh (250 mesh, 0.12 mm), titanium mesh (200 mesh, 0.15 mm), and copper foil (20 μm) were all purchased from SaiBo company. The GF/F separator (thickness: 420 μm; porosity: ≥90%; average pore size: 0.7 μm) was purchased from the Whatman company.

Preparation of electrolytes and electrodes

The $Zn(OTf)_2$–H_2O and $Zn(OTf)_2$–DEG electrolytes were prepared by directly adding $Zn(OTf)_2$ powders to H_2O and H_2O–DEG (2:1, molar ratio) with molar concentrations of 2 M, respectively. MASSE was formulated by homogenizing a mixture of $Zn(OTf)_2$–DEG electrolyte and 10 wt% Al_2O_3 nanoparticles using an ultrasonic cell grinder (400 W, 1 h), yielding a milky-white suspension. The PANI electrodes were prepared by combining 80 wt% active material, 10 wt% Ketjen Black, and 10 wt% PTFE dispersion in isopropanol to form a homogeneous paste, followed by rolling into free-standing films and subsequent thermal treatment at 60 °C for 8 h under vacuum conditions. Electrodes were affixed onto the stainless-steel mesh for electrochemical testing. Zinc metal was employed directly as the negative electrode without further treatment.

Characterizations

SEM measurements were performed with a Hitachi S-4800 field emission scanning electron microscope. XRD patterns of the samples were employed on an X'Pert Pro diffractometer utilizing monochromatized Cu K_α radiation (λ = 1.5406 Å) at a scanning rate of 10° min^{-1}. FTIR spectra were acquired using a Nicolet iS50 FTIR spectrometer integrated with a high-sensitivity diamond ATR accessory. Synchrotron radiation EXAFS was employed at the BL11B beamline of the Shanghai Synchrotron Radiation Facility. X-ray photoelectron spectroscopy was performed using a Thermo-Fisher Scientific ESCALAB Xi X-ray photoelectron spectrometer equipped with an Al K_α X-ray source (1486.68 eV). For depth profiling, a gas cluster ion beam source with 1 keV ion energy was employed to sputter 1 × 1 mm^2 regions, with the analysis focused on 200 × 200 μm^2 areas centered within these zones. Time-of-flight secondary ion mass spectrometry (TOF-SIMS) analyses were conducted using a TOF-SIMS5-100 system with a Cs^+ primary ion beam operating at 1 keV energy and a sample current of ~40 nA. Secondary ion signals were acquired over 1600 s from a 50 × 50 μm^2 analysis area, maintaining spatial resolution through controlled sputtering parameters. LSCM was performed on FV1000MPE. The in situ detection of hydrogen production was accomplished using China Education Au light in conjunction with a gas chromatograph (GC-7920, China) equipped with detection capabilities. The temperature change of the pouch cells during charging was monitored on an infrared thermal imager (FLIR T540, Sweden).

Electrochemical measurements

The electrochemical performances of the Zn||Zn, Zn||Cu, and Zn||PANI cells were examined using CR2032-type coin cells (case and spring material: stainless steel), conducted on a battery test station (LANHE CT3001A). Zn||PANI full cells were assembled using zinc foil (Φ12 mm) as the negative electrode and PANI (Φ10 mm) as the positive electrode. For standard coin cell evaluations, a 100-μm-thick Zn foil served as the negative electrode, paired with a PANI positive electrode having a mass loading of 1 mg cm^{-2}. For the high DOD cells tests, the 10-μm-thick Zn foil thermally pressed onto titanium mesh was used as the negative electrode, and the polyaniline (PANI) positive electrode had a loading of 12 mg cm^{-2}, with an N/P ratio of ~2. A standardized electrolyte volume of 120 μL was dispensed into each cell. Pouch cells were assembled by stacking a positive electrode of PANI (14 × 11 cm^2, 3 mg cm^{-2}) with Zn foils (15 × 12 cm^2, 10 μm). The positive electrode used stainless steel mesh as the current collector and tabs, while the negative electrode utilized zinc metal. One piece of positive electrode and two pieces of Zn foils are stacked together and encapsulated by aluminum plastic film through a vacuum final sealing machine (MSK-115A-L, Shenzhen Kejing Star Technology). The electrolyte volume of 8 mL was dispensed into each pouch cell. The stack pressure for pouch cells was ~300 kPa. The HT performance of cells was evaluated in a temperature-controlled incubator. All cells were placed in a climatic chamber for 1 h to achieve thermal equilibrium before performing electrochemical testing at different temperatures. The cut-off potentials for Zn||PANI cells were configured as 0.5 V and 1.5 V, and the current applied was varied in accordance with the experimental requirements, ranging from 0.5 to 8 A g^{-1}. LSV, chronoamperometry (CA), Tafel polarization test, and EIS were performed on the electrochemical workstation (CHI 760E). EIS tests were employed under potentiostatic conditions with a frequency range from 0.01 Hz to 100 kHz. The measurements were recorded with 12 data points per decade following a 2-s stabilization period at the open-circuit potential. Tafel tests were performed at a scan rate of 1 mV s^{-1} using Zn||Zn cells. LSV tests were conducted using Zn||Cu cells at a scan rate of 1 mV s^{-1} from −0.5 to 2.5 V (vs. Zn/Zn^{2+}). CA curves were recorded at a constant overpotential of 10 mV using Zn||Zn cells. The Zn^{2+} transference number was calculated according to the typical Evans method, as

presented by the subsequent equation:

$$\tau_{Zn^{2+}} = \frac{I_S(\Delta V - I_0 R_0)}{I_0(\Delta V - I_s R_s)} \quad (1)$$

where I_0/I_s and R_0/R_s represent the initial/final current density and charge transfer resistance before and after the polarization test, ΔV (10 mV) is the constant polarization potential for the chronoamperometry test. The ionic conductivity of the electrolyte was measured using a standard 2032 coin cell with two stainless steel electrodes placed symmetrically at a set distance. AC impedance analysis from 10 mHz to 100 kHz with an amplitude of 10 mV was used, and the ionic conductivity was calculated with the following equation:

$$\sigma = \frac{l}{RS} \quad (2)$$

Where R is the resistance, and S and L are the area and spacing between the electrodes, respectively. Data points from 20 to 140 °C were measured, and the symmetrical cells remained at a set temperature controlled for 30 min prior to the test.

DFT calculations

All calculations were performed with the Gaussian 16, C01 software package. The hybrid functional PBE0, coupled with the D3 dispersion correction of Grimme featuring Becke–Johnson damping (DFT-D3BJ), was employed throughout all calculations. For geometric optimization and vibrational frequency analysis, the def2-SVPD basis set was utilized, while the def2-TZVPD basis set was adopted for single-point energy calculations. The interaction energy between H_2O, DEG, and Al_2O_3 was calculated by the following equation:

$$E_{\text{binding energy}} = E_{\text{species}} + E_{\text{slab}} - E_{\text{slab/species}} \quad (3)$$

Where E_{species} and E_{slab} were the total energy of the adsorbate and bare surface directly obtained from DFT calculations, respectively, and $E_{\text{slab/species}}$ was the total energy of the optimized adsorbate-surface.

MD simulations

MD simulations were executed using GROMACS software. Three system-specific simulation boxes with optimized dimensions were generated based on molecular composition and stoichiometry. Following system construction, energy minimization was performed using the steepest descent algorithm with a force tolerance of 1000 kJ mol^{-1} nm^{-1}. Subsequent equilibration protocols included 100 ps temperature regulation (353.15 K) in the NVT ensemble and 100 ps pressure stabilization (1 atm) in the NPT ensemble. The production phase comprised 50 ns unconstrained MD trajectories.

Data availability

All data supporting the findings of this study are available within the article and the Supplementary Information file. Source data are provided with this paper.

References

1. Li, C., Jin, S., Archer, L. A. & Nazar, L. F. Toward practical aqueous zinc-ion batteries for electrochemical energy storage. *Joule* **6**, 1733–1738 (2022).
2. Hao, B. et al. Concentration polarization induced phase rigidification in ultralow salt colloid chemistry to stabilize cryogenic Zn batteries. *Nat. Commun.* **15**, 9465 (2024).
3. Innocenti, A., Bresser, D., Garche, J. & Passerini, S. A critical discussion of the current availability of lithium and zinc for use in batteries. *Nat. Commun.* **15**, 4068 (2024).
4. Wang, D. et al. Bidentate coordination enables anions-regulated solvation structure for advanced aqueous zinc metal batteries. *Angew. Chem. Int. Ed.* **64**, e202414117 (2024).
5. Wang, J. et al. Working aqueous Zn metal batteries at 100 °C. *ACS Nano* **16**, 15770–15778 (2022).
6. Zeng, X.-X. et al. An amphipathic ionic sieve membrane for durable and dendrite-free zinc-ion batteries. *Renewables* **2**, 52–60 (2024).
7. Chen, M. et al. Aqueous zinc-ion batteries at extreme temperature: mechanisms, challenges, and strategies. *Energy Storage Mater.* **51**, 683–718 (2022).
8. Yao, L. et al. Reconstruction of zinc-metal battery solvation structures operating from -50 ~ +100 °C. *Nat. Commun.* **15**, 6249 (2024).
9. Chen, Q., Chen, S., Ma, J., Ding, S. & Zhang, J. Synergic anchoring of Fe_2N nanoclusters on porous carbon to enhance reversible conversion of iodine for high-temperature zinc-iodine battery. *Nano Energy* **117**, 108897 (2023).
10. Lee, D. et al. Water-repellent ionic liquid skinny gels customized for aqueous Zn-ion battery anodes. *Adv. Funct. Mater.* **31**, 2103850 (2021).
11. Ming, F. et al. Co-solvent electrolyte engineering for stable anode-free zinc metal batteries. *J. Am. Chem. Soc.* **144**, 7160–7170 (2022).
12. Zhao, M. et al. Simultaneously stabilizing both electrodes and electrolytes by a self-separating organometallics interface for high-performance zinc-Ion batteries at wide temperatures. *Adv. Mater.* **34**, e2206239 (2022).
13. Zhao, M. et al. Semi-immobilized ionic liquid regulator with fast kinetics toward highly stable zinc anode under -35 to 60 °C. *Adv. Mater.* **34**, e2203153 (2022).
14. Wang, Y. et al. Solvent control of water O–H bonds for highly reversible zinc ion batteries. *Nat. Commun.* **14**, 2720 (2023).
15. Bai, X. et al. Eutectic-electrolyte-enabled zinc metal batteries towards wide temperature and voltage windows. *Energy Environ. Sci.* **17**, 7330–7341 (2024).
16. Huang, S. et al. Molecular crowding agent modified polyanionic gel electrolyte for zinc Ion batteries operating at 100 °C. *Adv. Funct. Mater.* **35**, 2419153 (2024).
17. Qiu, M. et al. Entropy-driven hydrated eutectic electrolytes with diverse solvation configurations for all-temperature Zn-ion batteries. *Angew. Chem. Int. Ed.* **63**, e202407012 (2024).
18. Qu, G. et al. A temperature self-adaptive electrolyte for wide-temperature aqueous zinc-ion batteries. *Adv. Mater.* **36**, e2400370 (2024).
19. Liu, Q., Li, J., Xing, D., Zhou, Y. & Yan, F. Ternary eutectic electrolyte for flexible wide-temperature zinc-ion batteries from -20 °C to 70 °C. *Angew. Chem. Int. Ed.* **64**, e202414728 (2024).
20. Zhang, R. et al. Weakly solvating aqueous-based electrolyte facilitated by a soft co-solvent for extreme temperature operations of zinc-ion batteries. *Energy Environ. Sci.* **17**, 4569–4581 (2024).
21. Deng, R. et al. "Soggy-Sand" chemistry for high-voltage aqueous zinc-ion batteries. *Adv. Mater.* **36**, 2311153 (2024).
22. Wang, L. et al. Cation-in-mesopore complex for 20 Ah-level aqueous battery. *Angew. Chem. Int. Ed.* **64**, e202501010 (2025).
23. Deng, S. et al. Zwitterion-separated ion pair dominated additive-electrolyte structure for ultra-stable aqueous zinc ion batteries. *Adv. Funct. Mater.* **34**, 2408546 (2024).
24. Xu, M. et al. Bicontinuous-phase electrolyte for a highly reversible Zn metal anode working at ultralow temperature. *Energy Environ. Sci.* **17**, 8966–8977 (2024).
25. Yang, M. et al. Boosting cathode activity and anode stability of Zn-S batteries in aqueous media through cosolvent-catalyst synergy. *Angew. Chem. Int. Ed.* **61**, e202212666 (2022).
26. Ma, C. et al. Dual-parasitic effect enables highly reversible zn metal anode for ultralong 25,000 cycles aqueous zinc-ion batteries. *Nano Lett.* **24**, 4020–4028 (2024).

27. Deng, R. et al. An aqueous electrolyte densified by perovskite SrTiO(3) enabling high-voltage zinc-ion batteries. *Nat. Commun.* **14**, 4981 (2023).
28. Peng, H. et al. Solvation modulation and reversible SiO_2-enriched interphase enabled by deep eutectic sol electrolytes for low-temperature zinc metal batteries. *Adv. Energy Mater.* **14**, 2302411 (2024).
29. Chen, Q. et al. Built-in trimodal molecular interaction effect enables interface-compatible and temperature-tolerance aqueous zinc batteries. *Adv. Funct. Mater.* **34**, 2406386 (2024).
30. Zhong, X. et al. Flexible zinc-air batteries with ampere-hour capacities and wide-temperature adaptabilities. *Adv. Mater.* **35**, e2209980 (2023).
31. Ren, H. et al. Molecular-crowding effect mimicking cold-resistant plants to stabilize the zinc anode with wider service temperature range. *Adv. Mater.* **35**, e2208237 (2023).
32. Xie, Z. et al. Carbonate-assisted chaotropic electrolyte for zinc ion battery with wide temperature operation. *ACS Energy Lett.* **9**, 3380–3390 (2024).
33. Jiao, M. et al. A polarized gel electrolyte for wide-temperature flexible zinc-air batteries. *Angew. Chem. Int. Ed.* **62**, e202301114 (2023).
34. Li, Y. et al. A novel ultrathin multiple-kinetics-enhanced polymer electrolyte editing enabled wide-temperature fast-charging solid-state zinc metal batteries. *Adv. Funct. Mater.* **34**, 2307736 (2023).
35. Zhuang, C. et al. Synergistic effect enables aqueous zinc-ion batteries to operate at high temperatures. *Adv. Funct. Mater.* **35**, 2419351 (2024).
36. Zhou, J. et al. Highly reversible and stable Zn metal anode under wide temperature conditions enabled by modulating electrolyte chemistry. *Chem. Eng. J.* **442**, 136218 (2022).
37. Wang, R. et al. An aqueous electrolyte regulator for highly stable zinc anode under −35 to 65 °C. *Adv. Energy Mater.* **13**, 2302543 (2023).
38. Wang, Z. et al. Chaotropic salt-aided "water-in-organic" electrolyte for highly reversible zinc-ion batteries across a wide temperature range. *Adv. Funct. Mater.* **34**, 2311271 (2023).
39. Yao, R. et al. A corrosion-free zinc metal battery with an ultra-thin zinc anode and high depth of discharge. *Energy Environ. Sci.* **17**, 3112–3122 (2024).
40. Wan, J. et al. Hydrated eutectic electrolyte induced bilayer interphase for high-performance aqueous Zn-ion batteries with 100 °C wide-temperature range. *Adv. Mater.* **36**, e2310623 (2024).

Acknowledgements

This work was supported by the Strategic Priority Research Program of the Chinese Academy of Sciences (XDB0600400, Z.C.), the Science and Technology Major Project of Liaoning Province (2024JH1/11700013, Z.C.), DICP Innovation Funding (DICP-I202433, D.W.), and National Natural Science Foundation of China (22402202, J.Z.), Vacuum Interconnected Nanotech Workstation (Nano-X), Suzhou Institute of Nano-Tech and Nano-Bionics, Chinese Academy of Sciences.

Author contributions

D.W. conceived ideas and designed experiments. J.R. conducted and analyzed the main experiments and authored the preliminary manuscript. J.Z. helped with the in situ experiments. Y.C. executed the pouch cell assembly. R.L. helped with data analysis. C.L. engaged in the theoretical simulation analysis. D.L. and X.G. offered suggestions about experiments. D.W. and Z.C. directed and supervised the study.

Competing interests

The authors declare no competing interests.

Additional information

Supplementary information The online version contains supplementary material available at https://doi.org/10.1038/s41467-025-67020-z.

Correspondence and requests for materials should be addressed to Dongdong Wang or Zhongwei Chen.

Peer review information *Nature Communications* thanks Xing-Long Wu and the other, anonymous, reviewer(s) for their contribution to the peer review of this work. [A peer review file is available].